

Journal of Biomedical Optics

BiomedicalOptics.SPIEDigitalLibrary.org

***In vivo* super-resolution retinal imaging through virtually structured detection**

Changgeng Liu
Yanan Zhi
Benquan Wang
Damber Thapa
YanJun Chen
Minhaj Alam
Yiming Lu
Xincheng Yao

SPIE.

Changgeng Liu, Yanan Zhi, Benquan Wang, Damber Thapa, YanJun Chen, Minhaj Alam, Yiming Lu, Xincheng Yao, "*In vivo* super-resolution retinal imaging through virtually structured detection," *J. Biomed. Opt.* **21**(12), 120502 (2016), doi: 10.1117/1.JBO.21.12.120502.

In vivo super-resolution retinal imaging through virtually structured detection

Changgeng Liu,^{a,†} Yanan Zhi,^{a,†} Benquan Wang,^a
Damber Thapa,^a Yanjun Chen,^a Minhaj Alam,^a
Yiming Lu,^a and Xincheng Yao^{a,b,*}

^aUniversity of Illinois at Chicago, Department of Bioengineering, 851 South Morgan Street, Chicago, Illinois 60607, United States

^bUniversity of Illinois at Chicago, Department of Ophthalmology and Visual Sciences, 1905 West Taylor Street, Chicago, Illinois 60612, United States

Abstract. High resolution is important for sensitive detection of subtle distortions of retinal morphology at an early stage of eye diseases. We demonstrate virtually structured detection (VSD) as a feasible method to achieve *in vivo* super-resolution ophthalmoscopy. A line-scanning strategy was employed to achieve a super-resolution imaging speed up to 127 frames/s with a frame size of 512×512 pixels. The proof-of-concept experiment was performed on anesthetized frogs. VSD-based super-resolution images reveal individual photoreceptors and nerve fiber bundles unambiguously. Both image contrast and signal-to-noise ratio are significantly improved due to the VSD implementation.

© 2016 Society of Photo-Optical Instrumentation Engineers (SPIE) [DOI: 10.1117/1.JBO.21.12.120502]

Keywords: retina; photoreceptor; super-resolution microscopy, structured illumination microscopy; ophthalmoscopy.

Paper 160676LR received Sep. 30, 2016; accepted for publication Nov. 28, 2016; published online Dec. 19, 2016.

Fundus photography plays a key role in retinal study and disease diagnosis. However, the diffraction limit poses a fundamental barrier to the spatial resolution of conventional ophthalmic instruments. Particularly, the maximum of available numeric aperture (NA) of the human eye is ~ 0.25 , which limits the spatial resolution of *in vivo* retinal imaging. Adaptive optics has been used to compensate for optical aberrations to improve resolution of retinal imaging,¹ but the achievable resolution is still diffraction limited. Further improvement of imaging resolution is desirable for sensitive detection of subtle distortions of retinal morphology at an early stage of eye diseases. Several approaches, including stimulated emission depletion microscopy,² photoactivated localization microscopy^{3,4} and stochastic optical reconstruction microscopy,⁵ have been demonstrated for high-resolution microscopy of biological cells and tissues. However, the high power requirement of laser illumination for super-resolution imaging limits their application for retinal study of living animals or humans. Moreover, all of these methods require

fluorescence labeling, which makes their application for imaging intrinsic optical signals (IOSs) unachievable. Structured illumination microscopy (SIM) performs a patterned illumination on the object to shift the high frequency information to lower frequencies within the passing bandwidth of the imaging system, and thus expands the effective bandwidth of the optical system by subsequent frequency shifting and recombination. SIM is applicable to both fluorescence^{6–8} and nonfluorescence imaging.^{9,10} However, for the purpose of super-resolution reconstruction, traditional SIM requires sophisticated mechanical manipulation of a grating^{9,10} or grid^{11,12} to generate structured illumination patterns with accurate phase control, which is particularly challenging for moving samples, such as the retina with inevitable eye movements. In theory, SIM also can be achieved in a point scanning system through spatiotemporal modulation, either by modulating the light source intensity in an illumination light path or by moving a physical mask in a detection light path.¹³ However, the physically spatiotemporal modulation of the illumination/detection light is difficult for ophthalmic applications due to the limited imaging speed.

We recently demonstrated super-resolution scanning laser microscopy¹⁴ using virtually structured detection (VSD), which requires neither physical modulation of the light source intensity in the illumination arm nor a physical mask in the light detection arm. Without the complexity of SIM for precise phase and pattern controls, the VSD-based approach provides an easy, low-cost, and phase-artifact-free strategy to achieve super-resolution scanning laser microscopy and optical coherence tomography.¹⁵ However, deployable application of the VSD for *in vivo* retinal imaging is challenged by limited frame-speed of single-point scanning prototype.¹⁴ Line-scanning strategy has been demonstrated for high-speed *in vivo* retinal imaging.¹⁶ Recently, we demonstrated the potential of combining the line-scanning strategy for VSD-based super-resolution imaging.^{17,18} In this letter, we report experimental validation of VSD combined with the line-scanning strategy as a feasible method to achieve *in vivo* super-resolution imaging of frog retina with subcellular resolution. Technical details of the VSD method and VSD-based line-scanning super-resolution imaging have been reported previously.^{17,19}

Figure 1 shows a schematic diagram of the experimental setup. A near-infrared superluminescent diode (SLD-35-HP, SUPERLUM), which has a center wavelength of 830 nm and a bandwidth of 60 nm, was used as the light source. A focused line illumination was produced by a cylindrical lens with a focal length of 50 mm. The focused line was scanned across the retina by a scanning galvanometer mirror (GVS001, THORLABS). The pivot point of the scanner was placed conjugate with the pupil plane of the frog eye to minimize the vignetting effect. The reflected light from the retina was descanned by the scanning mirror and relayed to the image plane of the retina with a magnification of ~ 43.55 . For theoretical estimation of system magnification, the focal length of the frog eye is assumed as ~ 2.87 mm.²⁰ A high-speed two-dimensional (2-D) CMOS camera with a pixel size of $20 \mu\text{m} \times 20 \mu\text{m}$ (Photron FastCam AX50) was used to acquire the images of the line profiles on the retina. The $20 \mu\text{m} \times 20 \mu\text{m}$ pixel size corresponds to a pixel sampling resolution of $0.46 \mu\text{m} \times 0.46 \mu\text{m}$ at the retina. To achieve the maximum imaging speed, only one-dimensional line scanning (along the y axis) was adopted, and nonisotropic resolution improvement would be expected. A region of interest

*Address all correspondence to: Xincheng Yao, E-mail: xcy@uic.edu

[†]These authors contributed equally to this work.

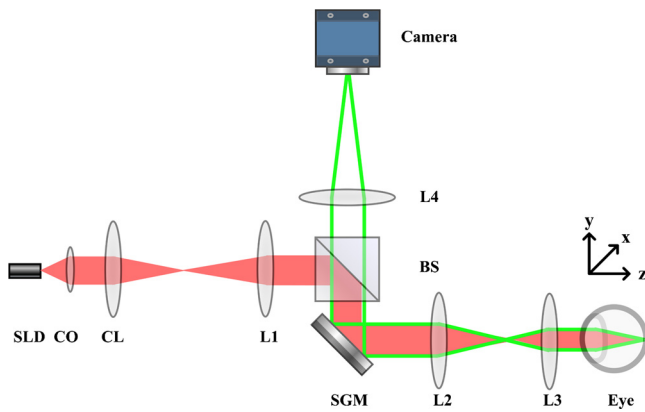


Fig. 1 Schematic diagram of the optical apparatus for *in vivo* imaging of frog retina. SLD, superluminescent diode; CO, collimator; L1–L4, lens; BS, beam splitter; CL, cylindrical lens; SGM, scanning galvanometer mirror. The scanning direction is along the y axis. The focal length of the CL is 50 mm. Focal lengths of lenses L1–L4 are 80, 80, 25, and 400 mm, respectively. The focal length of the frog eye is estimated as ~ 2.87 mm.²⁰ The pixel size of the camera is $20\ \mu\text{m} \times 20\ \mu\text{m}$.

of the camera, 32 pixels along the y direction and 512 pixels along the x direction, was chosen in the experiment. 512 line profiles were acquired to reconstruct one VSD-based super-resolution image. In our experiment, the imaging speed of the camera was set at 76,500 frames/s (fps), corresponding to a 127-fps speed for VSD-based super-resolution imaging. The light enters the frog pupil with a beam diameter of ~ 2 mm and a power of ~ 2.5 mW.

Northern leopard frogs (*Rana pipiens*) were used for this study. The experimental procedure was approved by the Office of Animal Care and Institutional Biosafety Committee of the University of Illinois at Chicago. The frog was anesthetized by immersing it into tricaine methanesulfonate (MS-222) solution (800 mg/l). After confirmation of the anesthesia, the frog was placed in an animal holder, which can provide five degrees of freedom to allow easy adjustment of the animal orientation and retinal area, to perform *in vivo* imaging. The pupils were fully dilated with atropine (1%) and phenylephrine (2.5%) solution.

Figure 2 shows representative *in vivo* images of the frog retinal photoreceptor layer. Figure 2(a) shows an equivalent wide-field image by superimposing raw images acquired with line-scanning illumination. The field of view is $\sim 207\ \mu\text{m} \times 207\ \mu\text{m}$. Because the photoreceptors can be barely resolved, the average size of the visible photoreceptor that is $\sim 6\ \mu\text{m}$ can be estimated as the actual resolution of the imaging system. Figure 2(b) shows the corresponding VSD-based super-resolution image. Spatial resolution along the y direction shows significant enhancement compared to the wide-field image as shown in Fig. 2(a). That is, the photoreceptors become readily resolved along the y direction, while along the x direction, they are still not well resolved, as evidenced by reflective intensity profiles shown in Figs. 2(c) and 2(d). Figure 2(c) shows the reflective intensity profiles along the horizontal (x direction) yellow dashed lines in Figs. 2(a) and 2(b), where we can see that the five individual photoreceptors could be barely resolved for both wide-field and VSD-based super-resolution images. The reflective intensity profile along the vertical (y direction) yellow dashed line in the VSD-based image shows significant improvement in terms of resolution compared to the counterpart in the wide-field image, as shown in Fig. 2(d). To confirm this

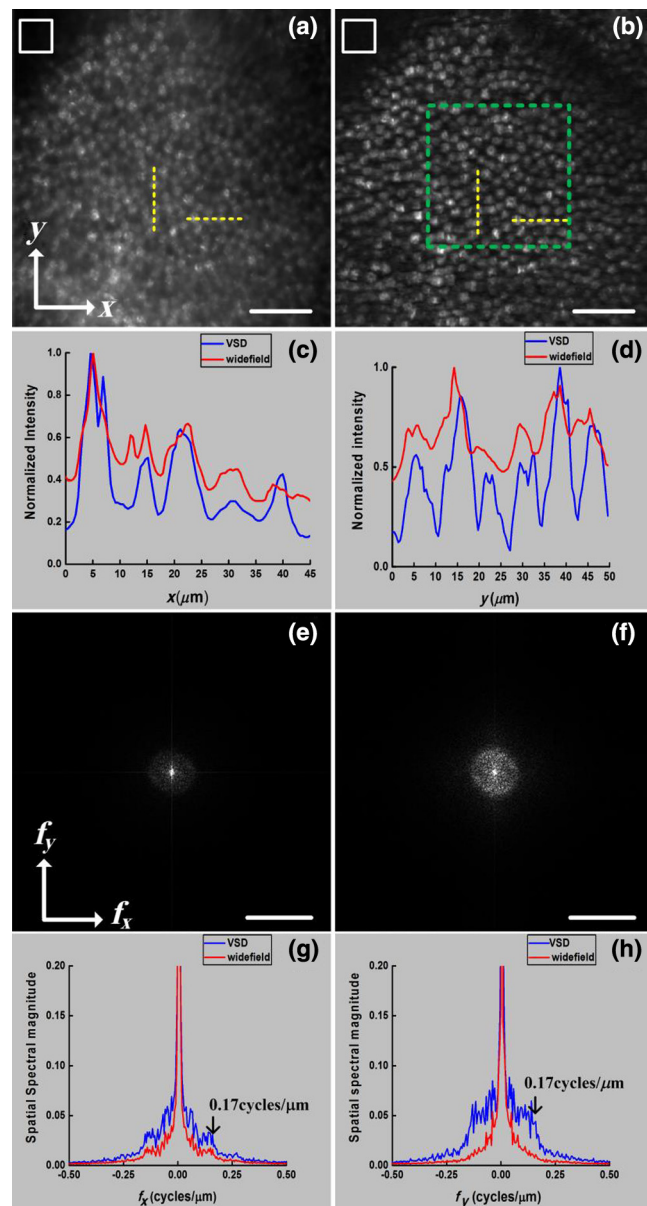


Fig. 2 Comparative *in vivo* imaging of the photoreceptor layer of the frog retina. (a) Equivalent wide-field image and (b) VSD-based super-resolution image. (c) Reflective intensity profiles along the horizontal yellow dashed lines in (a) and (b). (d) Reflective intensity profiles along the vertical yellow lines in (a) and (b). (e, f) spatial frequency spectra of (a) and (b), respectively. (g) Spatial frequency profiles along f_x direction through the centers of (e) and (f). (h) Spatial frequency profiles along f_y direction through the centers of (e) and (f). Scale bars in Figs. 2(a) and 2(b): $40\ \mu\text{m}$. Scale bars in Figs. 2(e) and 2(f): $0.5\ \text{cycles}/\mu\text{m}$.

perspective, we quantitatively compared spatial frequency spectra of the equivalent wide-field and VSD-based super-resolution images, which are shown in Figs. 2(e) and 2(f). It appears that the spatial frequency spectrum of the VSD-based image undergoes significant enhancement along both directions compared to the spatial frequency spectrum of the wide-field image. To clarify this point, we plotted the spatial frequency profiles of the spatial spectra along f_x and f_y (spatial frequency coordinates) directions in Figs. 2(g) and 2(h). Figure 2(g) shows the spatial frequency components along f_x direction of the VSD-based super-resolution image, which show slight improvement

compared to those of the wide-field image. The spatial frequency components along f_y direction of the VSD-based image, however, show significant improvement compared to those of the wide-field image, especially the spatial frequency components higher than $0.17 \text{ cycles}/\mu\text{m}$, which corresponds to the actual resolution, as evidenced in Fig. 2(h). The anisotropy of the spatial frequency enhancement confirms anisotropy of the spatial resolution improvement, which can be attributed to the unidirectional VSD implementation.

The benefit of the resolution enhancement can be shown in Fig. 3, which shows the zoomed view of the region marked by the green window in Fig. 2(b). Bright subcellular structures (red arrowheads) can be unambiguously observed. The bright subcellular structures were previously observed in two-photon excited autofluorescence images, which were speculated to be correlated with the structure of photoreceptor connecting cilium.²¹ Compared to the equivalent wide-field image, the VSD super-resolution image also showed improved signal-to-noise ratio (SNR) and image contrast. In order to calculate the image contrast of the wide-field images, and VSD-based super-resolution images, respectively, the images are divided into M overlapping segments and the maximum intensity I_{\max} and minimum intensity I_{\min} are found within the segmented region. The average contrast is calculated using

$$C = \frac{1}{M} \sum_{m=1}^M \frac{I_{\max} - I_{\min}}{I_{\max} + I_{\min}}. \quad (1)$$

The average contrasts of the equivalent wide-field image in Fig. 2(a), and the VSD-based super-resolution image in Fig. 2(b) are calculated as 0.54 and 0.92, respectively. Compared with the wide-field image, the VSD-based super-resolution image could obtain the clearer mosaic structure with higher image contrast. The SNRs of the equivalent wide-field and VSD-based super-resolution images can be estimated by

$$\text{SNR} = 20 \log \left(\frac{S}{N} \right), \quad (2)$$

where S is computed by averaging the peak intensities of the bright subcellular structures as highlighted in Fig. 3, and N

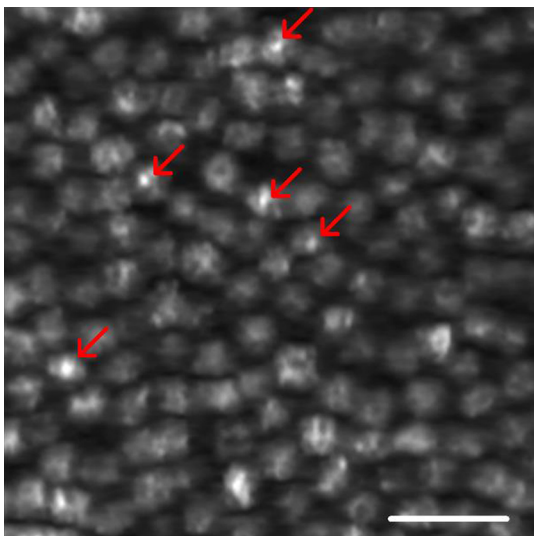


Fig. 3 Zoomed view of the region bounded by the green square in Fig. 2(b). Red arrows point to subcellular structures. Scale bar: $20 \mu\text{m}$.

is estimated by the standard deviation of the dark regions in the white boxes in Figs. 2(a) and 2(b). The SNR calculated from the wide-field image is $\sim 33 \text{ dB}$, while the SNR of the VSD-based image is $\sim 42 \text{ dB}$, which verifies that the SNR is also improved by the VSD method compared to the wide-field imaging.

To further confirm the improvement of spatial resolution and depth-resolved sectioning capability provided by the VSD method, frog retinal nerve fibers were also imaged. Figure 4 shows representative *in vivo* images of the frog retinal nerve fiber layer. Figures 4(a) and 4(b) show the wide-field and VSD-based images, respectively. It is clear that the VSD-based image shows significant improvement of spatial resolution compared to the wide-field image. Again the spatial frequency spectra of the wide-field and VSD-based images, as shown in Figs. 4(c) and 4(d), were quantified to confirm this observation. Similar to the case of the photoreceptor imaging, spatial frequency spectra of the VSD-based super-resolution image appear enhanced along both f_x and f_y directions compared to those of the equivalent wide-field image. By close examination of their spatial frequency profiles as shown in Figs. 4(e) and 4(f), it shows that improvement of the frequency components especially those higher than $0.17 \text{ cycles}/\mu\text{m}$ is indeed achieved mainly along

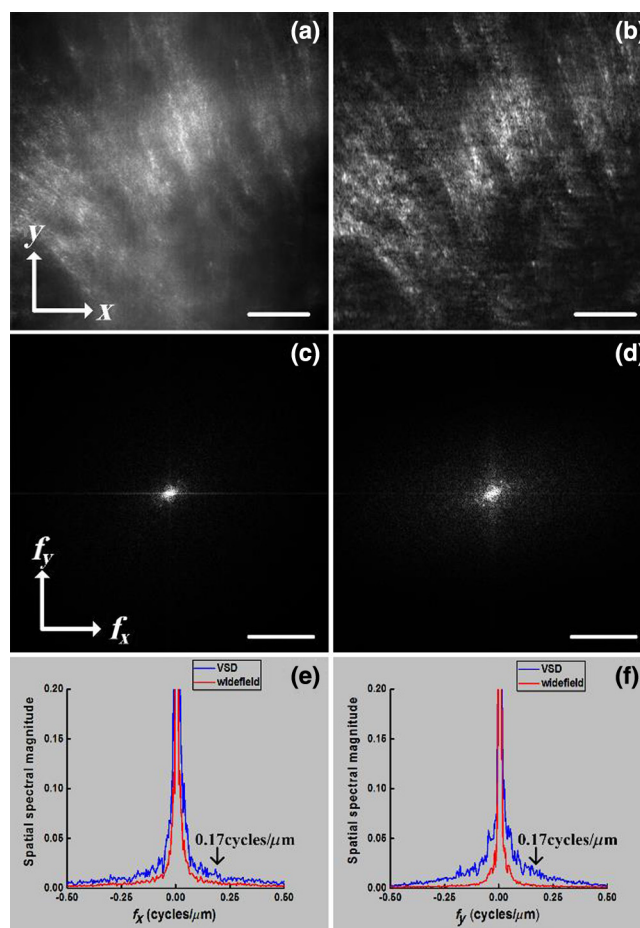


Fig. 4 Comparative *in vivo* images of the retinal nerve fibers. (a) Equivalent wide-field image and (b) VSD-based super-resolution image. (c, d) Spatial frequency spectra of (a) and (b), respectively. (e) Spatial frequency profiles along f_x direction through the centers of (c) and (d). (f) Spatial frequency profiles along f_y direction through the centers of (c) and (d). Scale bars in Figs. 4(a) and 2(b): $40 \mu\text{m}$. Scale bars in Figs. 4(c) and 2(d): $0.5 \text{ cycles}/\mu\text{m}$.

f_y direction, which is consistent with our observation in the photoreceptor imaging. This anisotropy reasonably arises from the unidirectional VSD implementation.

In summary, *in vivo* VSD-based super-resolution imaging of frog retina has been demonstrated using a high-speed line-scanning imager. In comparison with equivalent wide-field images, the VSD-based super-resolution images show improved spatial resolution, SNR, and image contrast. With improved resolution, subcellular structures, i.e., bright subcellular spots in retinal photoreceptors could be unambiguously identified (Fig. 3). According to comparisons of the extents of spatial frequency contents before and after VSD implementation, as evidenced in Figs. 2(g) and 2(h), and in Figs. 4(e) and 4(f), the resolution achieved by VSD-based line-scanning imaging is improved by a factor of $\sim 1.6\times$ compared to that of the wide-field counterpart. Further improvement in the extent of spatial frequency contents or spatial resolution begins to introduce imaging artifacts due to image noise. We are currently pursuing denoising methods to achieve further resolution improvement. For the proof of concept, the line-scanning strategy was employed to achieve image speed up to 127 fps, with a frame size of 512×512 pixels. In principle, the image speed can be further improved by decreased frame size. Because of the line illumination, the resolution improvement of the current prototype instrument is anisotropic. Isotropic resolution improvement can be achieved by using multiple-orientation scanning,¹⁷ with compromised image speed. Further development of the VSD-based imaging system can provide an easy, low-cost, and phase-artifact-free strategy to achieve super-resolution of the human retina, promising sensitive detection of morphological distortions to foster better study and diagnosis of eye diseases. Improved imaging resolution can also benefit functional assessment of retinal physiology. Recent studies have indicated that high resolution is essential to provide high sensitivity in functional IOS imaging of stimulus-evoked retinal physiological changes.^{22–24} Moreover, the development of super-resolution ophthalmic instruments will allow *in vivo* study of transient retinal phototropism,^{25–27} which can not only provide a better understanding of the nature of the visual system but may also produce new biomarkers for early detection of eye diseases.

Disclosures

No conflicts of interest, financial or otherwise, are declared by the authors.

Acknowledgments

This research was supported in part by NIH R01 EY023522, NIH R01 EY024628, NSF CBET-1055889, and NIH P30 EY001792.

References

1. D. R. Williams, "Imaging single cells in the living retina," *Vision Res.* **51**, 1379–1396 (2011).
2. S. W. Hell, "Toward fluorescence nanoscopy," *Nat. Biotechnol.* **21**, 1347–1355 (2003).
3. E. Betzig et al., "Imaging intracellular fluorescent proteins at nanometer resolution," *Science* **313**, 1642–1645 (2006).
4. M. F. Juetten et al., "Three-dimensional sub-100 nm resolution fluorescence microscopy of thick samples," *Nat. Methods* **5**, 527–529 (2008).
5. M. J. Rust, M. Bates, and X. Zhuang, "Sub-diffraction-limit imaging by stochastic optical reconstruction microscopy (STORM)," *Nat. Methods*, **3**, 793–795 (2006).
6. M. G. Gustafsson, "Surpassing the lateral resolution limit by a factor of two using structured illumination microscopy," *J. Microsc.* **198**, 82–87 (2000).
7. M. G. Gustafsson, "Nonlinear structured-illumination microscopy: wide-field fluorescence imaging with theoretically unlimited resolution," *Proc. Natl. Acad. Sci. U. S. A.* **102**, 13081–13086 (2005).
8. M. G. Gustafsson et al., "Three-dimensional resolution doubling in wide-field fluorescence microscopy by structured illumination," *Biophys. J.* **94**, 4957–4970 (2008).
9. S. Chowdhury, A. H. Dhalla, and J. Izatt, "Structured oblique illumination microscopy for enhanced resolution imaging of non-fluorescent, coherently scattering samples," *Biomed. Opt. Express* **3**, 1841–1854 (2012).
10. J. H. Park, J. Y. Lee, and E. S. Lee, "Enhancing the isotropy of lateral resolution in coherent structured illumination microscopy," *Biomed. Opt. Express* **5**, 1895–1912 (2014).
11. D. Debarre et al., "Adaptive optics for structured illumination microscopy," *Opt. Express* **16**, 9290–9305 (2008).
12. D. Karadaglic and T. Wilson, "Image formation in structured illumination wide-field fluorescence microscopy," *Micron* **39**, 808–818 (2008).
13. J. Lu et al., "Super-resolution laser scanning microscopy through spatiotemporal modulation," *Nano Lett.* **9**, 3883–3889 (2009).
14. R. W. Lu et al., "Super-resolution scanning laser microscopy through virtually structured detection," *Biomed. Opt. Express* **4**, 1673–1682 (2013).
15. B. Wang et al., "Breaking diffraction limit of lateral resolution in optical coherence tomography," *Quant. Imaging Med. Surg.* **3**, 243–248 (2013).
16. Q. X. Zhang et al., "In vivo confocal intrinsic optical signal identification of localized retinal dysfunction," *Invest. Ophthalmol. Vis. Sci.* **53**, 8139–8145 (2012).
17. Y. Zhi et al., "Rapid super-resolution line-scanning microscopy through virtually structured detection," *Opt. Lett.* **40**, 1683–1686 (2015).
18. X. C. Yao, R. W. Lu, and B. Q. Wang, "Super-resolution scanning through virtually structured detection," USA Provisional Patent, PCT# 61933987 (2014).
19. Y. Zhi, B. Wang, and X. C. Yao, "Super-resolution scanning laser microscopy based on virtually structured detection," *Crit. Rev. Biomed. Eng.* **43**, 297–322 (2015).
20. A. C. Aho, "The visual acuity of the frog (*Rana pipiens*)," *J. Comp. Physiol. A* **180**, 19–24 (1997).
21. R. W. Lu et al., "Two-photon excited autofluorescence imaging of freshly isolated frog retinas," *Biomed. Opt. Express* **2**, 1494–1503 (2011).
22. Q. Zhang et al., "Functional optical coherence tomography enables *in vivo* physiological assessment of retinal rod and cone photoreceptors," *Sci. Rep.* **5**, 9595 (2015).
23. X. Yao and B. Wang, "Intrinsic optical signal imaging of retinal physiology: a review," *J. Biomed. Opt.* **20**, 090901 (2015).
24. B. Wang et al., "En face optical coherence tomography of transient light response at photoreceptor outer segments in living frog eyecup," *Opt. Lett.* **38**, 4526–4529 (2013).
25. X. Zhao et al., "Stimulus-evoked outer segment changes in rod photoreceptors," *J. Biomed. Opt.* **21**, 065006 (2016).
26. B. Q. Wang et al., "Functional optical coherence tomography reveals transient phototropic change of photoreceptor outer segments," *Opt. Lett.* **39**, 6923–6926 (2014).
27. R. W. Lu et al., "Dynamic near infrared imaging reveals transient phototropic change in retinal rod photoreceptors," *J. Biomed. Opt.* **18**, 106013 (2013).